Elasmoid fish scales as a natural fiber composite: microscopic heterogeneities in structure, mineral distribution, and mechanical properties

Yiming Tan¹, Zian Jia¹, Zhifei Deng^{1,*}, and Ling Li^{1,2,*}

- 1. Department of Mechanical Engineering, Virginia Polytechnic Institute and State University, 635 Prices Fork Road, Blacksburg, VA 24061 USA.
- 2. Department of Materials Science and Engineering, University of Pennsylvania, 3231 Walnut St, Philadelphia, PA 19104 USA.
- * To whom correspondence should be addressed. E-mails: dengzf94@vt.edu, lzli@seas.upenn.edu.

Abstract

The elasmoid scales in teleost fish serve as exemplary models for natural fiber composites with integrated flexibility and protection. Yet, limited research has been focused on the potential structural, chemical, and mechanical heterogeneity within individual scales. This study presents systematic characterizations of the elasmoid scales from black drum fish (Pogonias cromis) at different zones within individual scales as a natural fiber composite, focusing on the microscopic structural heterogeneities and corresponding mechanical effects. The focus field at the center of the scales exhibits a classical tri-layered collagen-based composite design, consisting of the mineralized outermost limiting layer, external elasmodine layer in the middle, and the unmineralized internal elasmodine layer. In comparison, the rostral field at the anterior end of the scales exhibits a two-layered design: the mineralized outermost limiting layer exhibits radii sections on the outer surface and the inner elasmodine layer consists of collagen fiber-based sublayers with alternating mineralization levels. Chemical and nanoindentation analysis suggests a close correlation between the mineralization levels and the local nanomechanical properties. Comparative finite element modeling shows that the rostral field scales achieve increased flexibility under both concave and convex bending. Moreover, the evolving geometries of isolated Mandle's corpuscles in the internal elasmodine layer, transitioning from irregular shapes to faceted octahedrons, suggest the mechanisms of mineral growth and space-filling to thicken the mineralized layers in scales during growth, which enhances the bonding strength between the adjacent collagen fiber layers. This work offers new insights into the structural variations in individual elasmoid scales, providing strategies for bioinspired fiber composite designs with local-adapted functional requirements.

1. Introduction

Biological materials, which exhibit complex and hierarchical architectures, are increasingly serving as models and sources of inspiration for scientists and engineers [1–3]. The natural protection given by biological structural materials is the result of millions of years of evolution. As one of the representative biological materials, fish scales can be used as a model for designing new protective materials and structures with good combined mechanical properties, including flexibility, strength, and toughness [4–6].

There are four major types of fish scales: (i) ganoid, (ii) placoid, (iii) cycloid, and (iv) ctenoid [7–9]. The ganoid scales have a dense bony foundation with an enamel-like ganoine surface, which are found in a few freshwater fish, such as alligator gars [10] and Senegal bichir [11]. The placoid scales are commonly found in cartilaginous fish (e.g., sharks, rays, and skates), which show tooth-like dermal denticles with riblets and longitudinal grooves for hydrodynamic functions [7]. In comparison, both cycloid and ctenoid scales belong to the collagen-based elasmoid scales, commonly found in teleosts [12,13]. The elasmoid scales have concentric rings (circuli) on the outer surface, symbolizing the annual growth of the fish similar to tree rings [12]; the cycloid scales have these circuli with no interruptions, while the ctenoid scales have comb-like structures at the posterior margins. Among the different types of fish scales, the elasmoid scales represent the most abundant type in living fish. This collagen-based composite is often mineralized (primarily by hydroxyapatite) in the outer layers to resist penetration and hence to enhance protection [14]. Specifically, elasmoid scales can be considered as laminated composites with multilayered crossplywood structures, including the limiting layer (LL, mineralized), external elasmodine layer (EEL, partially mineralized), and internal elasmodine layer (IEL, unmineralized) [15-17]. Some studies also defined the combined LL and EEL as the external mineralized layer and considered the elasmoid fish scale as a bilayer composite. Together with the overlapping assembly, fish scales offer an excellent model system for developing fiber composite materials and flexible armor systems [18].

There have been many studies working on the structure-mechanical relationship in the elasmoid fish scales, and tension has been the most commonly used mechanical test to determine the strength and stiffness (Young's modulus) of fish scales. In general, the tensile response of elasmoid scales was linear at the initial stage, followed by plastic yielding before breakage, where the yielding is a direct result of the sliding and dissociation of collagen fibers [19]. Additional tensile studies of fish scales investigated the influence of scale location (over the fish body), mineral contents, fiber orientation, and hydration conditions [12]. For instance, Garrano *et al.* analyzed the tensile properties of *Cyprinus carpio* fish scales from several anatomical regions (head, body, and tail) as a function of moisture content in scales [20]. The strength and elastic modulus of the head scales were nearly double the values of tail scales when hydrated [20]; in contrast, no discernible variation was observed on the dehydrated scales [12]. Zhu *et al.* analyzed the arrangement of collagen fibrils and tensile strength of the scale of the striped bass (*Morone saxatilis*) [21]. The tensile strength and Young's moduli vary between 30 – 50 MPa and 600 – 850 MPa along 0°, 45°, and 90° from the longitudinal axis of the fish, respectively [21].

With the highest mineral level, the LL of the fish scale exhibits strong stiffness and hardness but undesirable brittleness [17,22]. Therefore, the exceptional fracture toughness of the scale composite is primarily due to the elasmodine layers (EEL and IEL) [18,21]. Dastjerdi *et al.* designed a customized fracture test configuration to probe the different fracture behaviors of fish scales, including fresh intact scales, collagen-only scales (by removing LL and EEL), and mineralized-only scales (by removing IEL) [23]. Specifically, small steel plates were clamped to the notched sample to transfer uniform loading and control crack growth. The results indicated that mineralized-only scales exhibited four times lower toughness than the collagen-only scales [23]. Moreover, the fiber orientations in the sublayers had a major influence on the directions of crack propagation, where the toughening mechanisms in the collagen layers involved massive defibrillation and crack bridging by the connecting fibers/ligaments [23].

The fish scale assembly achieves great combinations of protection and flexibility, which provide promising inspiration for multifunctional designs. For example, Rudykh *et al.* proposed a design map of scaled systems by investigating the design trade-off between flexibility and penetration resistance [24]. The design map was constructed based on the experimental results of 3D-printed models with an assembly of hard scales embedded in a soft matrix. The microstructural configurations were varied by changing the volume fraction and inclination angle of the slanted scales. The scale armor had the stiffest reaction at a soft/hard phase ratio of 1:1, and the indentation force decreased as the inclination angle increased [24]. Martini and Barthelat designed and manufactured the slanted scale system by gluing the engraved alumina plates onto the pre-strained polyurethane strip, which enhanced the puncture resistance and maintained the torsional and flexural flexibility [4]. In general, while the fish scale-inspired composites can resist penetration, they are also flexible due to the various deformation mechanisms, such as inter-plate matrix shear, plate rotation, and plate bending [24,25].

Previous studies on elasmoid fish scales focused primarily on the structure-mechanical properties of the entire scale as a layered composite with gradient properties. However, there is a lack of systematic characterization of the scales at the material level. The primary objective of this work is to characterize the structural, chemical, and mechanical properties at different zones of the individual scales from black drum fish (P. cromis) scales exemplifying the elasmoid scales. Specifically, three zones were selected along the longitudinal direction of the scales (see the three zones and corresponding abbreviations in **Fig. 1a-c**), including the focus field (F0, center of the circuli), the far end of the rostral field (R2, anterior end of the fish scale), and the middle between the focus and rostral end (R1). Corresponding comparative analysis including structural characterizations based on scanning electron microscopy (SEM) and microcomputed tomography (μ CT), chemical characterization using energy-dispersive X-ray spectroscopy (EDS), and multiscale mechanical characterizations via nanoindentation, comparative tension tests, and finite element modeling. The overall aim is to provide a multiscale characterization of the structure-property correlation of fish scales at different zones and provide a mechanical understanding of the structural variations in an individual scale for the effective bioinspired design of flexible armors.

2. Materials and Methods

2.1. Materials and sample preparation

The black drum fish (*P. cromis*) scales were obtained from Fruge Seafood Companies, Texas, USA. These scales were shipped in fresh condition and stored in frozen condition. After thawing and sonicated in deionized water, the selected scales were dried in air with heavy weights on top to minimize morphological changes. These scales were then cut into narrow strips along the longitudinal (anterior-to-posterior) and transversal (ventral-to-dorsal) directions (**Fig. 1a,b**) to minimize epoxy used for embedding (Epo-Fix, Electron Microscopy Sciences) and thus reduce the

influence of exothermic curing of epoxy. Those epoxy-embedded samples were used for elemental and nanoindentation characterizations. Sequential polishing was applied to the scale cross-sections using an automatic polishing machine (MultiPrep TM System, Allied HighTech Products, Inc.) with diamond lapping films (15 μ m, 9 μ m, 6 μ m, 3 μ m, and 1 μ m). The final procedure of surface finish involved cloth polishing with 40 nm colloidal silica suspension. Later, the samples were sonicated again in DI water to remove the remaining colloidal particles.

2.2. Scanning electron microscopy (SEM) and Energy-dispersive X-ray spectroscopy (EDS)

The scale samples were dried and then coated with a 10 nm Pd/Pt layer to reduce the charging effect before imaging. SEM images were acquired with an FEI Quanta 600 FEG environmental SEM with an acceleration voltage of 15 kV and a working distance of ~12 mm. The backscattered electron (BSE) images were acquired with a Bruker QUANTAX 400 XFlash 4010 (10 mm²) silicon drift detector. In addition, the SEM-EDS data were also obtained using the same scope with an acceleration voltage set at 20 kV. The elemental composition was quantified using the Bruker Esprit 2.1 Software with PB Linemarker-ZAF correction. Areal maps and line profiles were collected to reveal the distribution of the selected elements (Fig. 2), including the major elements of Phosphorus (P), Calcium (Ca), and trace elements of Carbon (C), Sulfur (S), Chlorine (Cl), Oxygen (O).

2.3. Synchrotron-based micro-computed X-ray tomography (μCT)

The μ CT measurements were conducted using synchrotron X-ray at beamline 2-BM of the Advanced Photon Source, Argonne National Laboratory, Chicago. The beam energy used was 27.4 keV. The camera imaging resolution was 1.30 μ m/pixel and a field of view (FOV) of 2560×1280 pixel², corresponding to ~3.33 mm in width and~1.66 mm in height. During the μ CT scans, the stage was rotated 180° to capture 1500 projection images for 3D reconstruction. Tomographic reconstructions were performed using TomoPy, segmented using the open-sourced machine-learning-based software Ilastik, and rendered with Avizo (Thermo Fisher Scientific, USA). Especially, Mandle's corpuscles (MC) were further labeled using the Random-Walk Distance Transformation module from AmiraZIBEdition (Thermo Fisher Scientific, Zuse Institute Berlin), which quantified the spatial and geometrical information of the isolated particles (**Fig. 4**, Figs. S8-10).

2.4. Nanoindentation

The nanoindentation property gradients on the polished fish scales were measured using an instrumented nanoindentation system (NanoTest Vantage platform 4, Micro-Materials, UK). Line mapping over the scale thickness was conducted using a Berkovich tip to examine hardness (H) and reduced modulus (E_r). The spacing between adjacent indents was 2 μ m, and the maximum load was 2 mN with a loading profile of loading (15 s), holding (10 s), and unloading (15 s). Thermal drifting was monitored for 30 s at the unloading stage when the load was unloaded to 10% of the maximum load (0.2 mN). The system was set to equilibrate for at least three hours prior to performing nanoindentation. For each sample, 3 lines were drawn on the rostral (R2, R1) and focus (F0) fields of the scale cross-sections for statistical purposes under dry conditions (relative room humidity level at ~30%, Fig. 5). Nanoindentation areal mapping was conducted on a selected radii section (RS) of a transversal cross-section (T-N plane) near the anterior end of the scale with spacing of $10 \times 10 \ \mu\text{m}^2$ per indent (R2 field, Fig. S11). For comparative purposes, linemapping nanoindentation was also conducted and analyzed under 90% relative humidity conditions (Figs. S12-S13).

2.5. Macroscopic uniaxial tension

The dogbone-shaped tensile samples were cut along the longitudinal and transversal directions using the customized steel cutting dies (WhiskyTime, Etsy, Inc.) from large fish scales (Figs. S14-S15). The gauge area was 40 mm² with dimensions of 4 mm in width and 10 mm in length. The average thickness of the samples was *ca.* 0.4-0.5 mm, and the measurement of the individual scales was used for the following analysis of the strength approximation. Demineralized scale samples were also prepared to investigate the mechanical contribution of the mineral phase. The demineralization protocol involved acid treatment by immersing the scale samples in 0.4 mol/L hydrochloric acid for 90 minutes (Fig. S15a) [26]. The acid-treated scales were then immersed in the artificial seawater solution for more than 24 hours before thickness measurements and tensile tests. The demineralization treatment was confirmed by SEM imaging, where the flattened surface circuli indicated the complete removal of minerals (Fig. S15g). In total, 40 scale samples were prepared with 10 samples for each direction (longitudinal *vs.* transversal) and condition (intact *vs.* demineralized). The uniaxial tensile tests were carried out on an Instron 6800 mechanical testing machine, with a load cell of 2 kN. The mechanical tests were performed at room temperature at a displacement rate of 0.2 mm/min, and the hydration of the samples was maintained by water spraying during the tests. The tensile results were presented in terms of engineering stress-strain curves, and the tensile properties were quantified including strength (maximum stress), modulus (linear fitting of the initial deformation), and energy (integration of the stress-strain profiles, **Fig. 6**).

2.6. Finite element (FE) simulation

Based on the characteristics of rostral and focus field structures of black drum scales, models for FE simulation were generated using Abaqus/CAE 6.14 (Fig. 7, Fig. S16-17). The dimensions of real-scale beam models with multilayer structures and various external surfaces were designed based on the optical and SEM images in R2, R1, and F0 regions of the scale (Fig. 7a): (1) The R2 field consisted of alternating collagen and mineralized layers (9) sublayers with decreasing thickness) with surface RS units; (2) the R1 field consisted of RS units in the LL, mineralized EEL, and collagen IEL; and (3) the F0 field consisted of mineralized LL and EEL with collagen IEL. The width of the beam models was 3.38 mm (10 RS units), and the thickness (or height) of the beam models corresponds to the measurements from the multilayered scale samples (i.e., 0.31 mm of the R2 and R1 models, and 0.35 mm of the F0 models, Fig. 7a). 3D models were configured by extruding along the out-of-plane direction with thickness of 0.5 mm (Fig. S16). For direct comparison, the comparative models C2, C1, and C0 with simple multilayered structures were generated with the same thickness in alternating mineralized and collagen layers (Fig. 7b). The 8-node linear brick, decreased integration, and hourglass control elements (C3D8R) were used in FE beam simulations. Each beam model had 1 million quadrilateral mesh elements. The material property inputs in the FE modeling were obtained from the tensile tests. The strength (σ_c) and modulus (E_c) of the collagen layers were estimated from the tensile strength of demineralized scales, and the properties of the mineralized phase were determined based on the rule of mixture in composite materials,

$$E_{scale} = V_c E_c + V_m E_m \tag{Eq. 1},$$

where E_{scale} is the tensile modulus of intact scale, E_m is the modulus of the mineral phase, and $V_c \sim 0.4$ and $V_m \sim 0.6$ are the volume fraction of the collagen and mineral phases, respectively. It must be noted that the rule of mixture used here may not precisely predict the property correlations in fish scales, but the approximated modulus E_m here should be sufficient for comparative analysis of the multilayered designs in the following FE simulations. The strength of the mineralized phase σ_m was estimated as the strength of the intact scale σ_{scale} , where the maximum stress corresponded to the breakage failure of the mineralized phase. The Poisson's ratios of the collage fibers and HA were approximated as ca. 0.3 [27,28]. In FE modeling, the three-point bending load was applied to the central point until a maximum force of 100 N. Only half of the beam models were generated by taking advantage of the structural and loading symmetry, and the lateral edge of the beam models was fixed to the bottom or the top edge for the concave or convex bending, respectively (Fig. S16). The FE modeling was used to analyze the deformation capability of fish scales in different fields via von Mises stress distribution and displacement-load correlations.

3. Results

3.1. Microstructure

The surface and cross-sectional features were characterized systematically using SEM and μ CT images. First, the coordination and orientation systems of the fish scales are defined as shown in **Fig. 1a,b**. Based on the fish body anatomy, the anterior-posterior orientation is defined as the longitudinal (L) direction, the ventral-to-dorsal orientation is defined as the transversal (T) direction, and the normal (N) direction defines the orientation from the interior (proximal to body) to the exterior (distal to body) of the scale. On individual scales, the surface characteristics can be divided into five fields (**Fig. 1b**) [12], including the rostral field close to the anterior end (ca. 1/2 of the scale length), the focus field at the center (ca. 1/3 of the scale length and ca. 1/2 of the scale width), the caudal field at the posterior end (ca. 1/6 of the scale length), and two lateral fields close to the ventral and dorsal sides. The rostral, focus, and lateral fields are embedded underneath the overlapping scales, while only the caudal field is exposed.

The surface morphologies of the black drum fish scales reveal intricate surface characteristics at different fields (Fig. 1c-f, Fig. S1). First, the focus field is the initial part for scale growth, exhibiting labyrinthic patterns of surface ridges with microscopic ridge hierarchical features on those labyrinthic patterns (Fig. 1c,f). Ring-like circuli ridges exhibit parallel patterns surrounding the central focus region, which are the developed "growth rings" interrupted by the caudal field (Fig. 1c). On the rostral field of the scales, groove-like radii along the radial directions disrupt circuli ridges, where the primary radii extend from the focus field to the anterior end, and secondary radii initiate within the rostral field (Fig. 1c). In contrast, the circuli ridges are continuous with no interruptions in the lateral fields (Fig. S1b). The surface morphology difference between the circuli ridges at the rostral and lateral fields is that hierarchical protrusions on the ridges are only available at the rostral field (Fig. 1d,e) but not the lateral field (Fig. S1c). On the caudal field of the scales, the microstructures showed overlapping arrangements of the individual tubercles (ctenii) with sharpened tails, probably for hydrodynamic functions (Fig. S1d). In comparison, smaller scales exhibited similar structural features and field divisions to the larger scales; yet the focus field is much smaller and regular (Fig. S2).

In this study, the primary focus is to compare the structure designs at different zones of the fish scale. Three zones of interest were selected on the scale (**Fig. 1c**), including the rostral field close to the anterior end (R2), the focus field (F0), and the approximate middle between the anterior end and focus field (R1). As noted earlier, the surface circuli represent the growth rings of the scales with early-formed ridges close to the focus field and newly formed ones near the anterior end and lateral edges; that is, the R2 zone is the most recently formed region and F0 zone is the earliest formed region.

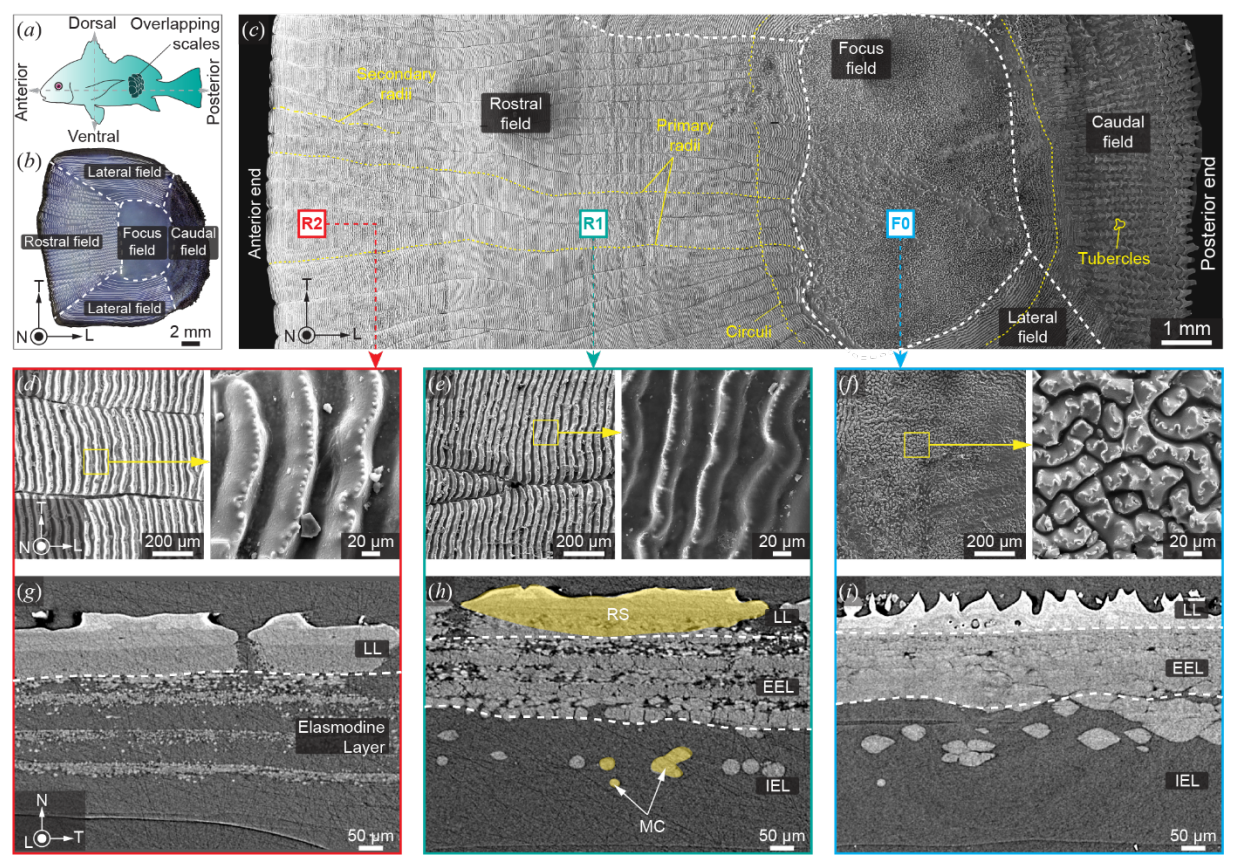


Figure 1. Structural characterization at different regions of black drum fish scales. (a,b) Coordinate definition of (a) the fish body and (b) individual scales, where the longitudinal (L) and transversal (T) directions are defined along the anterior-posterior and ventral-dorsal axes, respectively, and "N" denotes the normal direction. (c) SEM image of the selected region on a fish scale exhibiting the surface morphologies at rostral (R2, R1), focus field (F0), and caudal field, where R2 denotes a region close to the anterior end of the scale, F0 represents the focus field, and R1 resides at the middle between the R2 and F0 zones. (d-f) SEM images on the local surface morphologies of the (d) R2, (e) R1, and (f) F0 zones, respectively, where the zoom-in images highlight the microscopic circuli features and the nanoscopic protrusion on each circulus. (g-i) Vertical cross-sections of μ CT reconstruction of (g) R2, (h) R1, and (i) F0 zones on the transversal T-N planes of the fish scale, exhibiting different multilayered structures including the limiting layer (LL) and external and internal elasmodine layers (EEL + IEL), as well as the fusiform-like radii sections (RS) in the rostral field and the distributed mineralized Mandl's corpuscles (MC) in IEL.

Apart from the difference in surface morphologies between the rostral field (R2 and R1) and the focus field (F0), the multilayered features on the transversal cross-sections exhibit more interesting variations (**Fig. 1g-i**, Fig. S3-5). In general, the fish scale exhibits multilayered structures, which can be generally divided into three layers, including a limiting layer (LL, highest mineralization) and an elasmodine layer further divided into external and internal elasmodine layers based on the mineralization difference, as shown by the SEM images (Fig. S3) and μ -CT reconstructions (**Fig. 1g-i**, Fig. S4). In the outermost LL, fusiform-like radii sections (RS) are observed on the transversal cross-sections (*T-N* planes) of both the R2 and R1 zones, where the edges of the RS units correspond to the radii intercepting the circuli ridges (**Fig. 1g,h**). In the most developed F0 zone, the surface profile in the F0 zone has irregular morphologies, corresponding to the labyrinthic patterns in the focus field (Figs. S3d, S4d). The external

elasmodine layer (EEL) consists of collagen fibrous sheets with higher mineralization, and the internal elasmodine layer (IEL) is typically not mineralized. The collagen cross-ply layers exhibit orthogonal fiber bundles in the alternating layers and decreasing thickness toward the scale interior, as revealed by the high-resolution SEM images of the polished and dried scale samples (Fig. S5), which should correlate with the circumferential and radial fibers of the individual scale (**Fig. 3a,b**). In the newly formed R2 zone, no defined separation can be found between the external and internal elasmodine layers, where the micro- and nano-sized mineralized particles, named Mandl's corpuscles (MC) [29], are distributed with alternating high and low concentrations (**Fig. 1g**, Figs. S3b, S4b). Interestingly, it seems that the sublayers with fiber orientations parallel to the *L* direction have high concentrations of mineralized particles compared to the alternating in-plane fiber layer (fibers parallel to *T* direction), which can be evidenced by the electron density variations from the backscattered SEM image (Figs. S3b). At the macroscopic level within the individual scale, the sublayers with radial fibers should have a higher mineralization level than the circumferential fibers. Later, the R1 zone is developed with more defined boundaries between the EEL and IEL (**Fig. 1h**, Figs. S3c, S4c), where the MC particles in the EEL grow in size and channels to densify the mineralized phases and additional isolated MC particles float in the IEL. In the F0 zone, the mineralized particles become densely packed in the EEL, and isolated MC particles exhibit rhombus-shaped cross-sections and aggregates of multiple particles (**Fig. 1i**).

3.2. Chemical analysis

The elasmoid scales are composed of hydroxyapatite (HAP) and type-I collagen fiber sheets [30], which can be confirmed by the chemical characterizations (**Fig. 2**, Fig. S6). Based on the areal mapping at the focus field, the detected elements of interest include phosphate (P) and calcium (Ca) concentrated in the LL and EEL of the bulk scale, with highest concentrations in the LL (**Fig. 2b,c**). In comparison, no Ca or P is found in the IEL (except for the MC particles) due to the low mineralization content. Additional trace elements of sulfur (S) and chloride (Cl) are found with generally uniform distributions across the scale thickness (**Fig. 2d,e**).

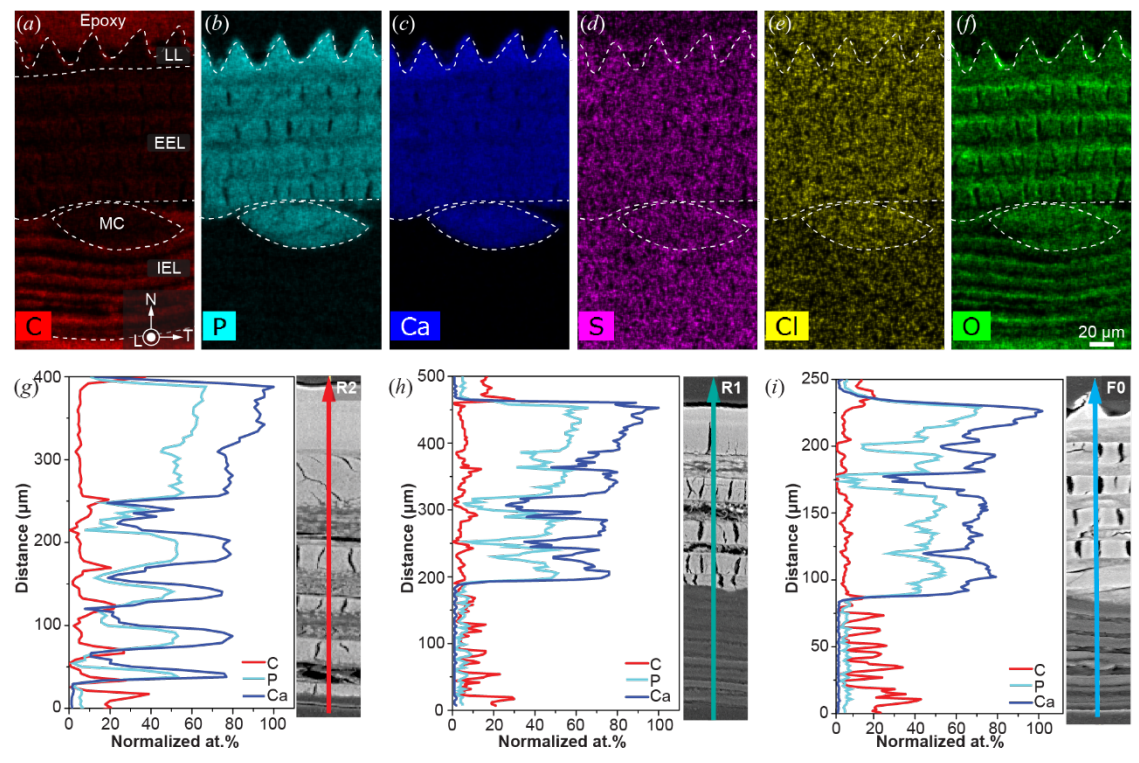


Figure 2. Chemical characterizations at different regions of black drum fish scales. (a-f) EDS elemental areal maps at the focus region, including major elements (C, P, and Ca) and trace elements (S, Cl, and O), respectively. (g-i) EDS line profiles of the selected major elements across the thickness of the fish scales at (g) R2, (h) R1, and (i) F0 zones, respectively. The line profiles of the element distributions are normalized by the maximum atomic percentage (at. %).

Comparative EDS line profiles were collected at R2, R1, and F0 zones to correlate with the multilayers across the scale thickness (**Fig. 2g-i**). In the R2 zone, P and Ca trends show a local increase with electron-dense regions in the multilayers; except for the LL, the higher mineralized alternating layers correspond to those with fiber orientations (along *L* direction) perpendicular to the plane of view (*T-N* plane, **Fig. 2g**). The elasmodine layer with high P and Ca exhibits similar levels of mineralization, which are slightly lower than the LL. In the R1 zone, higher P and Ca levels reside in LL and EEL (in total ~60% of scale thickness, **Fig. 2h**), showing a similar trend as in the R2 zone. A sharp drop of mineralization is observed across the boundary of EEL and IEL, with oscillating C levels in the collagen layers in IEL correlating with alternating fiber orientations. In the F0 zone, the general oscillating trends of the chemical elements P, Ca, and C agree with the trends in the R1 zone, with alternating high and low mineralization in the EEL and no mineralization in IEL (**Fig. 2i**).

3.3. Mandl's corpuscles

According to the above structural and chemical investigations, the LL and EEL constitute the majority of the mineralization in the black drum fish scales. Yet, the isolated mineral particles and aggregated assembly are present in the IEL. These MC particles can be revealed by SEM imaging on the scales after peeling off LL and EEL layers (Fig. 3).

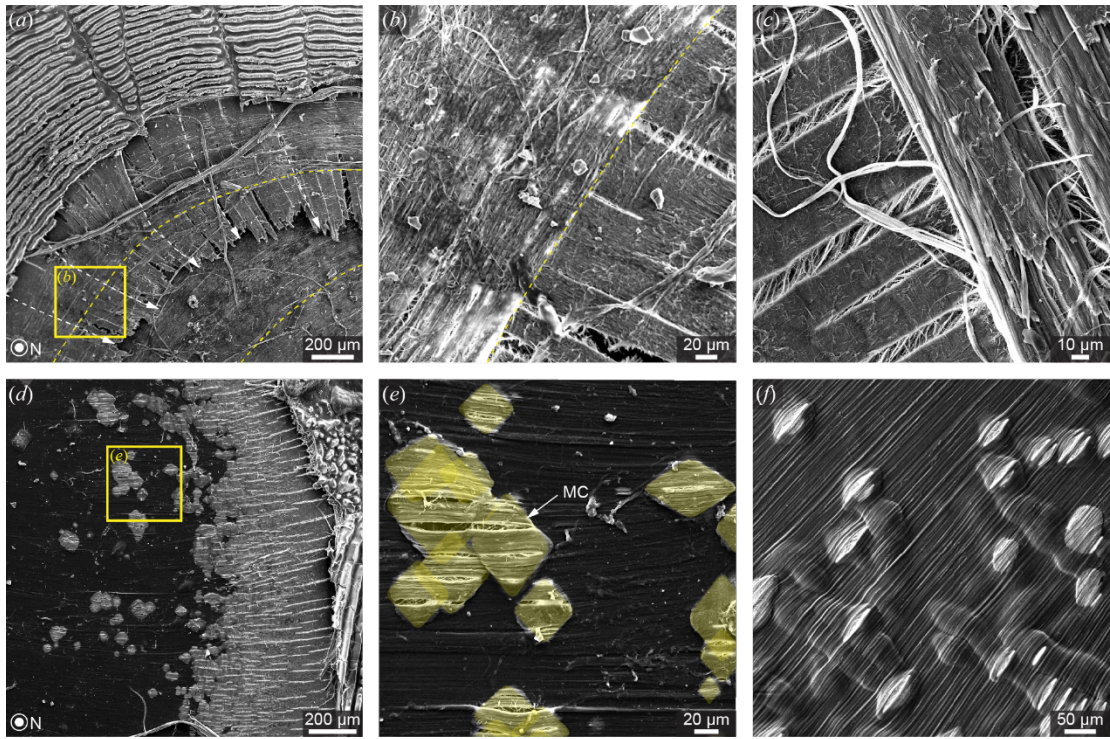


Figure 3. Fiber arrangement and mineralized particles exposed on the fractured fish scales. (a-c) SEM images of fractured fish scales, including **(a)** delamination failure exposing fibrous multilayers under the surface circuli and **(b,c)** orthogonal fiber arrangements. The yellow dashed lines trace the circumferential alignment of collagen fibers (surrounding the focus region), and the white dashed arrows point to the radial alignment of the fibers. **(d-f)** SEM images of fractured fish scales exposing **(d,e)** the aggregated clusters of rhombus-shaped mineralized MC particles with major axes along the local fiber orientation, and **(f)** corrugated sheets due to the local mineralization in the fibrous IEL.

On one hand, the peeling failure of the black drum fish scale induces delamination between the sublayers, which reveals the alternating circumferential and radial fiber orientations in adjacent layers of the bulk scale (**Fig. 3a**), forming orthogonal fiber alignment at the local scale (**Fig. 3b**). The fiber bundles act to bridge the cracks in the adjacent layers, which prevent premature failure (**Fig. 3c**). In comparison, the fractured surface near the outer circumference of the rostral and caudal fields reveals U-shaped fiber bundles pointing outward along radial directions (Fig. S7a-d). It is proposed that these U-shaped bundles persist along the entire outer circumference of the scales, forming local cross-ply structures in adjacent fibrous sheets (Fig. S7e). On the other hand, the mineral phases are

shown as the regions with higher electron density, where the isolated MC particles fall further away from the aggregates than the connected mineralization front (**Fig. 3d**). The mineral aggregates can be generally considered as a cluster of rhombus-shaped MC particles with their major axes (ca. 50-100 µm in dimensions) along and perpendicular to the local fiber orientations (**Fig. 3e**). The corrugated surface of the fibrous sheets after delamination failure suggests that these particles are not 2D features but 3D volumes, where volume expansion of these particles during mineralization deforms fibrous sheets in the IEL (**Fig. 3f**).

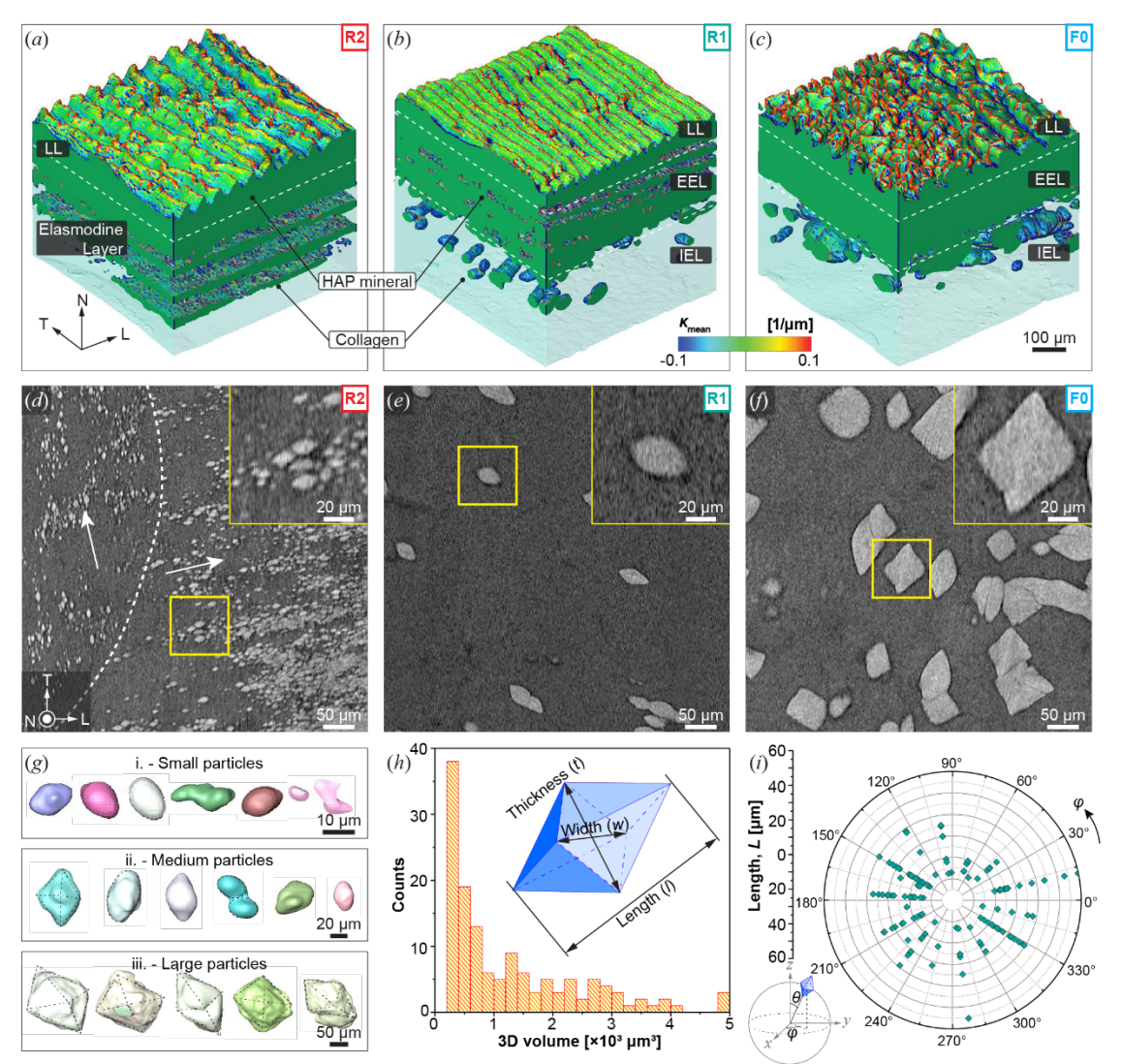


Figure 4. Synchrotron-based micro-computed X-ray tomography at different regions of black drum fish scales. (a-c) 3D reconstruction of the fish scale at (a) R2, (b) R1, and (c) F0 zones, where the mineralized layers and particles are colored with local surface mean curvatures ($-0.1 - 0.1 \, \mu m^{-1}$) and the collagen layers are shown in transparent mode to exhibit the distributed MC particles in IEL. (d-f) Horizontal slices of the fish scale at (d) R2, (e) R1, and (f) F0 zones, where the insets highlight the different morphologies of mineralized particles. The white arrows in (d) mark the perpendicular orientations of particle alignment in adjacent sublayers at the R2 zone. (g) 3D morphologies of the separated MC particles in the F0 zone, which can be generally classified into three categories (i) small particles with irregular features, (ii) medium particles with oval or faceted shapes formed by particle attachment, and (iii) large particles exhibiting octahedron faceted shapes. (h,i) Quantification of the separated MC particles, including (h) 3D volumes ($< 5 \times 10^3 \, \mu m^3$ only) and (i) particle lengths and in-plane distribution.

Detailed analysis of the distribution and 3D geometries of these MC particles was conducted using the synchrotron μ CT results (**Fig. 4**, Figs. S8-10). First, from the 3D rendering of the selected zones in fish scales, the distribution of mineral phases exhibits clear differences: (1) The newly formed R2 zone exhibits layered distribution in the

elasmodine layer with the innermost layer of mineralization merging by the micro-sized mineral particles (**Fig. 4a**, Fig. S8a,d). Here, it should be emphasized that the alternating mineralization does not originate from the local fiber orientations but truly correlated with the different mineral densities, as evidenced by the contrast between adjacent sublayers bordered by the white dashed line in **Fig. 4d**. (2) The R1 zone shows defined EEL with higher mineralization content, yet the mineralization is not fully densified but with remaining sites for further filling. The individual MC particles are sparsely distributed with ellipse-shaped particles (**Fig. 4b**, Fig. S8b,e). (3) The developed F0 zone shows fully mineralized EEL, and additional faceted octahedron MC particles are enlarged in IEL (> 50 µm in length) and aggregated to form clusters (**Fig. 4c**, Fig. S8c,f). From the surface curvature mapping, the MC particles exhibited mean curvatures below zero (**Fig. 4a-c**, Fig. S8d-f). Especially, the MC particles exhibited morphological evolution at different stages of mineralization, starting from ellipse particles (sizes of 1-10 µm) in the R2 zone (**Fig. 4d**), to enlarged ellipse (sizes of 20-30 µm) with some faceted boundaries in the R1 zone (**Fig. 4e**), and finally more regular faceted MC particles (major axes of *ca*. 50 µm) with edge merging (**Fig. 4f**). The 3D reconstruction of the isolated MC particles confirmed the 2D observation from the reconstructed slices, where the small irregular particles grow in size probably by layered deposition (to form medium-sized ellipses) and by particle attachment (to form irregular aggregates) and later develop into larger faceted particles with roughened edges (**Fig. 4g**).

Detailed characterization of the MC particles in a scale sample at the F0 zone was conducted to characterize the dimensions and orientations (Figs. S9, S10). After segmentation and 3D rendering, the geometrical parameters were characterized by length (l), width (w), thickness (t), and the 3D volumes of the individual MC particles (Fig. S10a). Excluding the larger particles (> 5×10³ μm³ probably due to particle merging), the remaining smaller particles were used for size distribution and orientation analysis. The counts of MC particles decrease exponentially as the particle size increases (Fig. 4h, Fig. S10c) For geometrical characterizations, while the thickness-to-width (t/w) ratio gives a normal distribution near 1.0, the length-to-width (l/w) ratio gives a skewed distribution with a maximum at 2 (Fig. S10d,e). Therefore, the individual MC particles exhibit equiaxed dimensions in the thickness-width plane and elongated morphology along the length axes. For orientation analysis, spherical coordinates with paired angles (θ, φ) were used to quantify the orientations of the length axes of the particles, where θ was the polar angle characterizing the out-of-plane orientations and φ was the azimuthal angle characterizing the in-plane orientations (Fig. S10b). First, the polar angle θ exhibits a centered distribution between ~78-86° (Fig. S10f), suggesting the in-plane distribution of the MC particles (with a slight offset tilting angle of $\sim 8^{\circ}$ against the analyzed plane). Second, the azimuthal angle φ , as well as the length l and l/w ratio, does not show preferred in-plane orientation in the range of 0-360° (Fig. 4i, Fig. S10g,h), confirming the alignment between the long axis of the MC particles and the local fiber orientations (completing a 360° rotation along the circumferential and radial directions in the fish scales).

3.4. Microscopic mechanical behavior: nanoindentation

The mineral phases have a close correlation with the mechanical behaviors of the fish scales at the material level. To probe the mechanical gradients across scale thickness, comparative nanoindentation line mapping was conducted at different zones (R2, R1, and F0) of the black drum fish scales (Fig. 5).

In general, close correlations were found between the property profiles and the distribution of mineralized phases along the scale thickness, with the highest reduced modulus (E_r) and hardness (H) in the LL and lowest in the collagenbased IEL (Table. S1). First, the property trends exhibit obvious oscillations in the R2 zone (Fig. 5a), where the cyclic undulation correlates with the high-and-low distribution of the mineralization levels as revealed by the EDS chemical mappings in Fig. 2g. The modulus and hardness show an obvious decrease from LL ($H = 1.2 \pm 0.6$ GPa, $E_r = 31.7 \pm 0.6$ 11.2 GPa) to the elasmodine layer, which oscillates between $H \sim 0.16 - 2.25$ GPa (average of 0.8 GPa) and $E_r \sim 9.2 -$ 36.0 GPa (average of 20.9 GPa). In comparison, the property profiles are quite similar in the R1 and F0 zones (Fig. 5b,c), with obvious oscillations in the EEL of the R1 zone (due to incomplete mineralization) but not in the EEL of the F0 zone (due to densified mineralization). Especially, the properties in the EEL ($H = 0.43 \pm 0.25$ GPa, $E_r = 13.54$ \pm 5.11 GPa) and IEL (H = 0.38 \pm 0.23 GPa, E_r = 7.31 \pm 1.94 GPa) show a stepwise decrease in the F0 zone. Considering that nanoindentation line mappings only measure the property gradients across the scale thickness, an additional area map was conducted on a highly mineralized RS unit of the R2 zone, which verified the uniform properties in the sublayers with the same fiber orientations (Fig. S11). Also, within the RS feature, E_r results did not vary significantly with fiber orientations in the adjacent sublayers ($E_r \sim 30\text{-}40 \text{ GPa}$), but the H map observed higher values in the sublayer with out-of-plane fibers ($H \sim 1$ GPa) than the in-plane fibers ($H \sim 0.5$ GPa), agreeing with the observation that the sublayers with out-of-plane fibers have higher electron density (Fig. S11a). Considering that in the fully developed Z0 field with fully densified mineralization in EEL, the hardness profile is almost constant (Fig. 5c), suggesting an ignorable difference in the mechanical contribution in the sublayers with in-plane and out-of-plane fibers. Therefore,

the property variations observed in the R2 and R1 zones should mostly correlate with the mineralization levels rather than fiber orientations.

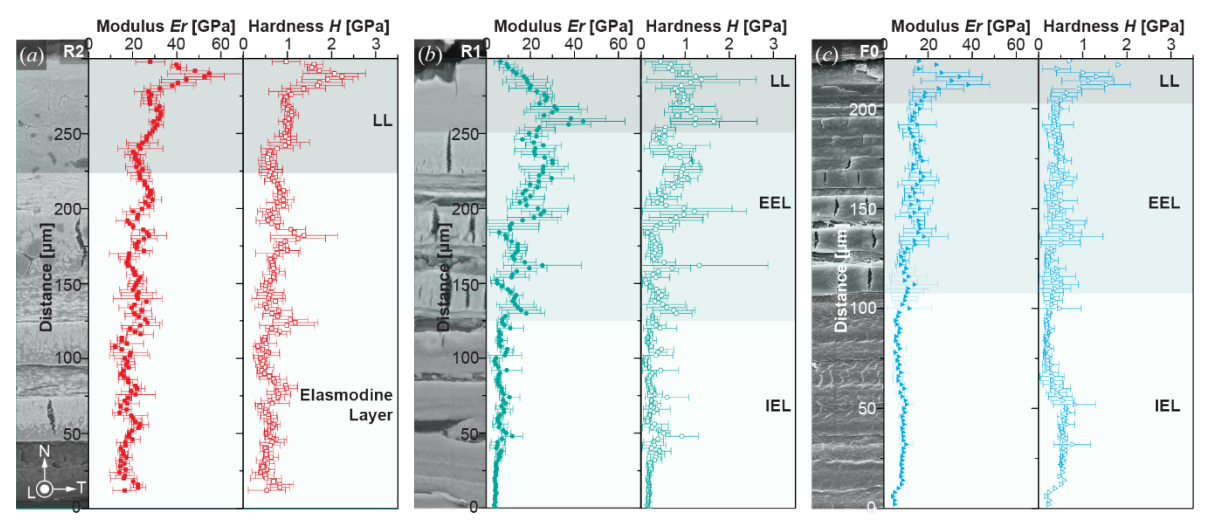


Figure 5. Nanoindentation properties along the thickness of fish scales at (a) R2, (b) R1, and (c) F0 zones, respectively, including reduced modulus (E_r) and hardness (H) under dry conditions (room humidity).

In addition, the comparative nanoindentation was also conducted under 90% relative air humidity conditions in the R1 and F0 zones of the fish scales (Fig. S12). The property profiles inherited the general trends with higher properties in the mineralized layers. At the R0 zone, while the LL layer maintained a similar hardness ($H \sim 0.13 - 3.75$ GPa, average of 0.97 GPa) and modulus ($E_r \sim 3.8 - 82.6$ GPa, average of 23.7 GPa) under increased humidity compared to the dry condition, the EEL ($H = 0.18 \pm 0.10$ GPa, $E_r = 6.29 \pm 2.50$ GPa) and IEL ($H = 0.06 \pm 0.04$ GPa, $E_r = 1.35 \pm 0.78$ GPa) showed a significant decrease due to the softening effect of the collagen-dominated constituents (Fig. S13, Table S1).

3.5. Macroscopic mechanical behavior: tension

The mineral contents and the cross-ply arrangements of the collagen fibers also have a close correlation to the mechanical behaviors of the fish scales. Therefore, comparative tensile tests were conducted to investigate the influence of testing orientations (longitudinal *vs.* transversal) and mineralization (intact *vs.* demineralized). **Fig. 6a,b** plots the stress-strain curves for tensile tests of dogbone samples along the longitudinal and transversal samples, while Fig. S14 and Fig. S15 compare the tensile tests of intact and demineralized samples, respectively.

First, the stress-strain curves of intact scales under tension along the longitudinal and transversal directions did not show obvious differences, both exhibiting classical polymer material behaviors before cracking of the mineralized layers. Cracks in LL initiated at the grooves of the surface circuli (regarded as pre-existing microscopic notches) parallel to the loading direction, and the cracked LL induced following delamination between the LL and the underlying elasmodine layers (**Fig. 6d**). From the post-failure samples, failure usually occurred near the clamped end due to the decreased thickness towards the scale circumference (Fig. S14d,e). The mineralized MC particles also act as bonding agents for the adjacent fiber bundles in individual layers (**Fig. 6e**) and adjacent cross-ply layers (**Fig. 6f**, Fig. S14f). This structural feature, by "gluing" fiber bundles together locally, is able to resist and/or deflect crack propagation around the MC particles in 3D (**Fig. 6g**). In addition, the non-mineralized IEL layer showed bridging fibers connecting the crack openings (**Fig. 6h**). The highly mineralized LL, however, exhibited brittle fracture exposing failure surfaces resembling typical "conchoidal fractures" observed in biominerals (Fig. S14g). The analyzed properties showed similar strength ($\sigma_{scale} \sim 50$ MPa) and failure energy ($W_{scale} \sim 5.4-6 \times 10^6$ J/m³) along the longitudinal and transversal directions under tensile tests, while only the tensile modulus measured statistically higher values along the transversal direction (**Fig. 6c**).

Second, for demineralized scale samples, no directional dependence was reported for the samples along the longitudinal and transversal directions regarding the tensile stress-strain curves and analyzed properties (Fig. S15). The mechanical equivalence along these two directions could correlate with the cross-ply arrangement of the fibrous

sheets in fish scales; with the circumferential and radial alignment of the collagen fibers at the macroscopic scale, we expect the demineralized scales to exhibit in-plane mechanical isotropy along any random orientations (Fig. S7). From the SEM images of the post-facture samples, failure also occurred near the clapping ends due to the reduced thickness there, where the fiber bundles exhibit bridging mechanisms and wrinkle after tensile failure (**Fig. 6h**, Fig. S15d-f). Based on the comparison of the analyzed properties, the demineralized samples exhibited sharp decreases in the tensile strength and modulus, suggesting the strengthening and stiffening effects of the mineral phases (**Fig. 6c**). However, the demineralized scales exhibited ~60% increased strain at maximum stress.

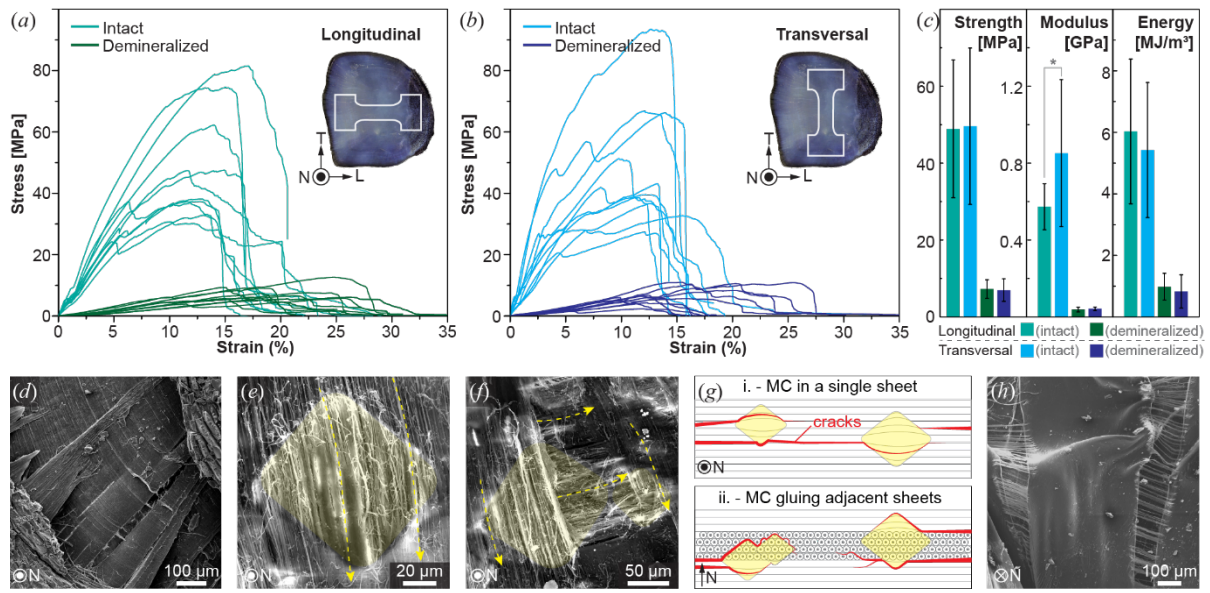


Figure 6. Comparative tensile tests of intact and demineralized black drum fish scales. (a,b) Stress-strain curves of the intact and demineralized scales along the (a) longitudinal and (b) transversal directions, respectively. (c) Comparative tensile results of different samples, including strength, modulus, and failure energy. The asterisk denotes a significant difference at a confidence level of 95%. (d) Top-view SEM images of the fractured scales, revealing fibrous sheet delamination from the mineralized layer. (e,f) SEM images of fractured collagen sheets with MC particles anchoring (e) in-plane fibers and (f) the adjacent fiber sheets with orthogonal fiber orientations, where the yellow rhombuses mark the MC particles and yellow dashed lines indicate the fiber orientations. (g) Schematics of crack arrest and deflection (red curves) in IEL, including (i) in-plane crack deflection along the curved fibers around the MC particles and (ii) out-of-plane crack deflection with MC particles binding adjacent sheets with orthogonal fibers. (h) Bottom-view SEM image of the failed intact scale, revealing the bridging mechanisms by collagen fibers in the IEL.

3.6. Macroscopic mechanical behavior: computational analysis

Previous structural, chemical, and nanomechanical characterizations revealed the intrinsic differences of different zones at the material level. In this section, to understand the mechanical differences of fish scales at the macroscopic level, FEM analysis was conducted at different zones. The multilayered structures with alternating high and low mineralization, as well as the different features in the LL, were replicated and standardized based on the SEM and μ CT images (**Fig. 1g-i**, Fig. S3) of the transversal cross-sections (on the *T-N* planes) of the scales at R2, R1, and F0 zones, respectively (real scale models in **Fig. 7a**). In addition, comparative multilayered beams without LL features (RS in the R2 and R1 zones and triangular corrugations in the F0 zone) were generated to investigate the influence of these surface features (C2, C1, and C0 models in **Fig. 7b**). Three-point bending was applied to the center of the scale-inspired models by applying load-controlled displacement to generate concave and convex bending, corresponding to bending from the scale exterior (**Fig. 7c-e**, Fig. S17a,b) and interior (**Fig. 7f-h**, Fig. S17c,d), respectively.

The specific questions to be answered include: (1) What are the mechanical adaptations of different zones in individual fish scales? (2) How do the mechanical designs of fish scales with specified multilayered structures and surface structures compare with simple multilayered structures? (3) What is the bending asymmetry under concave and convex bending? In the following paragraphs, the von Mises stress distribution and the displacement-load curves

are used for the comparison between the structural adaptations between the real scale models and later with the simple multilayered models. The results for the concave and convex bending cases are introduced separately, which are compared later to discuss the mechanical asymmetry under these two loadings.

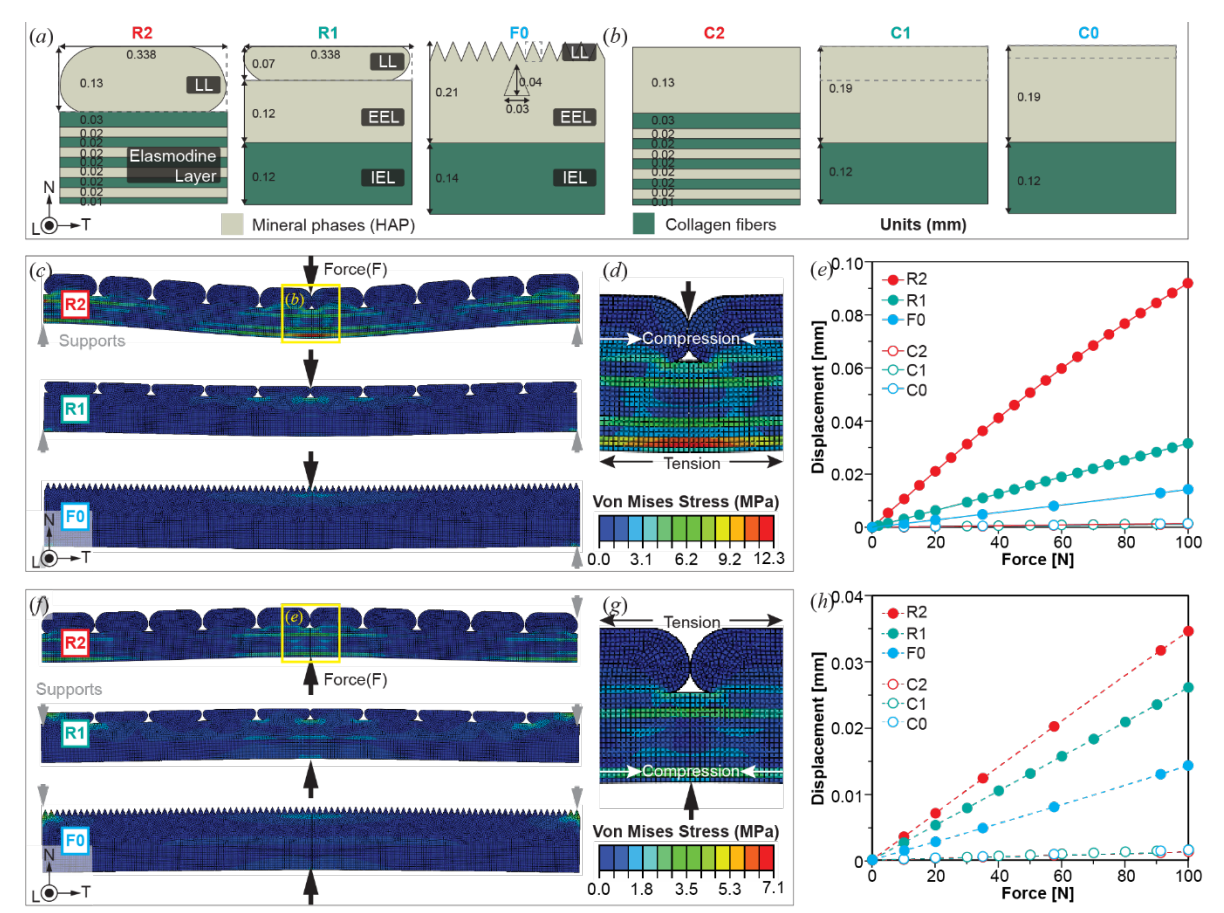


Figure 7. Finite element modeling results of fish scales under load-controlled three-point bending. (a,b) Geometrical models for finite element modeling, including (a) the real scale models at R2, R1, and F0 zones and (b) the comparative multilayered C2, C1, and C0 models consisting of alternative layers of mineralized and collagen layers. (c,d,f,g) Distribution of von Mises stress results in fish scales at R2, R1, and F0 zones under (c,d) concave bending (loading from outside) and (f,g) convex bending (loading from inside), respectively. (d,g) Zoom-in regions of the stress distribution at the contact region of the R2 zone under (d) concave and (g) convex bending, respectively. (e,h) Displacement-force profiles of the finite element beam models under (e) concave and (h) convex bending, respectively.

First, under concave bending, the bottom side of the scales (interior) is under tension while the scale exterior is under compression. The stress distribution and the displacement-load curves exhibit clear differences (**Fig. 7c-e**, Fig. S17a,b). Upon the maximum load of 100 N, the R2 zone exhibited the most significant displacement (0.092 mm) than the R1 and F0 zones, and the bottom surface of the R2 scale had the highest von Mises stress of 12.24 MPa due to easy tension of the collagen sublayers in elasmodine layer. The mineralized RS units ensured increased resistance against contact loading, while the grooves between RS units enabled spaces for compressive deformation (**Fig. 7d**). In comparison, the R1 and F0 scales with tri-layer structure (mineralized EEL and unmineralized IEL) and LL features showed lower deformability and the maximum stress occurs near the grooves of the surface features (RS in R1 scale and ridges in F0 scale) due to the local stress concentration (**Fig. 7c**). The comparison between R2 and R1 models suggests that multilayered collagen fibrous sheets with alternating high and low mineralization have the advantage of increasing deformability under concave bending. The comparative multilayered models (C2, C1, and C0) show much smaller deformation displacements and von Mises stresses (Fig. S17a,b), indicating that the surface features with grooves allowed compressive deformation without cracking the mineralized LL and thus increased deformability of

the entire scale. The maximum von Mises stress in the multilayered models all occurred underneath the contact point, which followed C0 > C2 > C1 although their differences were negligible.

Second, under convex bending, the general stress distribution is reversed with the scale interior under compression and the scale exterior under tension (**Fig. 7f-h**, Fig. S17c,d). The highest von Mises stress is found at the grooves of these surface features in all three real scale models, where the local stress concentration is induced by the tensile stress on the convex side (**Fig. 7f,g**). The comparison between the three real scale models suggests the order of flexibility R2 > R1 > F0 under convex bending (**Fig. 7h**), similar to the concave bending case. Such structural-chemical-mechanical adaptations at different regions of the scales could correlate with the functional requirements, where the newly formed R2 zone at the anterior end inserted into tissue shows the best flexibility, and the developed F0 zone of the scale overlaps to resist predator loading requiring higher stiffness and strength. The comparative multilayered models also exhibit much smaller stress and displacement compared to the real scale model under convex bending, confirming the increased flexibility by the surface structures regardless of the loading directions.

In addition, regarding the concave-convex bending asymmetry, the simple multilayered models show ignorable differences in the displacement curves (Fig. S17b,d). Yet, it is likely due to reduced flexibility by the flat mineralized layers reduces the deformability significantly and limits the deformation only within the elastic regime upon the maximum load of 100 N (displacement < 2×10⁻³ mm compared to beam thickness of 0.3 mm). In those cases, the displacement is mainly induced by the local deformation in the collagen layers rather than the entire beam models. Even in the R1 and F0 of the real scale models, the similar maximum displacement does not indicate obvious concave-convex bending asymmetry (**Fig. 7e,h**). This is mainly attributed to the elastic deformation in the beam models under both concave and convex bending with maximum stress below the yielding point of collagen ~7 MPa (**Table 1**); the deformation in the two scale models might not be significant enough upon 100 N to show the bending asymmetry. In comparison, the R2 zone exhibits approximately two times higher displacement under concave bending (0.92 mm) than the convex bending (0.35 mm). Such a difference could be mainly attributed to the material gradients. The key assumption for composite beams under bending is the linear distribution of bending strain over the section, which induces generally higher strains in the collagen layers. For the R2 scales, more portions of the collagen layers are under tensile stress when applied to concave bending, leading to more significant deformation.

4. Discussion

4.1. Mechanical comparison with different biological scale systems

Elasmoid fish scales consist of collagen and calcium-based minerals (primarily calcium phosphate, and calcite carbonate) [30]. The mineral-to-collagen weight ratio varies significantly in different species [7], e.g., 1:1.2 in red seabream [19] and 1:2 in the scutes of box fish [31]. Thus, as a combination of mineralized segments and soft matrix, scaled skin gives a combination of flexibility and protection. Also, the overlapping pattern of scales minimizes the drag during swimming through wave regulation about the body [32], and even contributes to effective undulatory locomotion through scales interlock and release [33]. **Table 1** compares the tensile results of elasmoid fish scales, where the 0° and 90°samples are defined as cut along and perpendicular to the long axis of the fish to study the inplane anisotropy [21,34]. Regardless of the large variations in shapes, sizes, and overlapping arrangements of the elasmoid scales, their tensile response and properties are rather similar. Yet, the strength and modulus of the *P. major* scale are roughly twice as high as those of the other elasmoid scales, which could be attributed to the higher mineral-to-collagen ratio in the scale thickness [19]. In addition, hydration has a significant effect on the properties of elasmoid scales, where the highly mineralized (HAP) fibers contributed to greatly increased stiffness and modulus under dry conditions [16,35], especially in the partially mineralized EEL as suggested by the comparative nanoindentation results (Fig. S14).

It should be noted that some fish scales exhibit anisotropic responses when loaded along different directions, which should correlate with the cross-ply orientations in the collagen fibrous matrix [36]. For example, the cross-ply orientations follow orthogonal directions (with 90° rotation) between consecutive layers in the scales of sea bream (*Pagrus major*) [19], striped bass (*Morone saxatilis*) [37], rainbow fish (*Poecilia reticulata*) [38], and black drum (*Pogonias cromis*) in this study (**Fig. 3a-c**). In comparison, Bouligand patterns with plywood-like layers completing 180° rotations across thickness direction were also reported, where the inter-ply angles could be irregular (e.g., (*Arapaima Gigas*) [34] and jewelfish (*Hemichromis bimaculatus*) [38]) or regular (e.g., 60° inter-ply angles in Atlantic tarpon *Megalops Atlanticus* scales [39], and 75° in the tarpon *Megalops atlanticus* and the carp *Cyprinus carpio* scales [36]). In addition, the coelacanth (*Latimeria chalumnae*) scales represent an interesting exception, which consist of two sets of Bouligand structures perpendicular and interpenetrating to each other [40,41].

Table 1. Tensile results of elasmoid scales under different conditions

Species	Scale type	Conditions	Directions	Strength (MPa)	Modulus (GPa)
Pogonias cromis (this work)	Ctenoid (intact)	Wet	0°	48.9 ± 17.9	0.57 ± 0.12
			90°	49.6 ± 20.3	0.85 ± 0.38
	Ctenoid	Wet	0°	7.3 ± 2.4	0.04 ± 0.01
	(demineralized)	WEL	90°	7.0 ± 2.9	0.04 ± 0.01
Arapaima Gigas [16,35]	Cycloid	Dry		46.7 - 53.85	1.2 - 1.38
		Wet		22.26 - 25.2	0.1 - 0.83
Pagrus major [19]	Cycloid	Wet	_	93 ± 1.8	2.2 ± 0.3
Megalops Atlanticus [39]	Ctenoid	Wet	0°	22.6 ± 5.1	0.22 ± 0.03
		Wet	0°	~32*	~0.85*
Morone saxatilis [21,37]	Ctenoid	Wet	45°	~48*	~0.62*
		Wet	90°	~52*	~0.8*
Cyprinus carpio [20]	Cycloid	Wet	0°	33.4 - 34.0	0.45 - 0.59
Latimeria chalumnae [41]	Elasmoid		0°	~50	~0.21
	(Cycloid)		90°	~50	~0.25

^{*} Note that some values in the table are estimated from the stress-strain curve.

As teleost fish scales are amongst the toughest biological materials known (15-18 kJ/m² for *M. saxatilis*) [23], the orthogonally-arranged collagen fiber lamellae provide increased toughness through different responses to the crack front in adjacent layers, *e.g.*, fracture, separation, and deflection, all contributing to stress delocalization [42]. Under tension, lamellae reorientation toward the tensile axis was observed under small angle X-ray scattering (SAXS) [43] and modeled considering the elastic stretching, strain-rate sensitivity, and inter-fibrillar sliding [34]. *In-situ* tensile tests on notched samples also revealed lamellae delamination as an energy-absorbing mechanism [34] and crack bridging as a prevailing toughening mechanism [8].

There are other models of flexible armor in nature, such as osteoderms from reptiles (armadillos, alligators, and turtles) and mammals (armadillo) [8], keratinous armor in pangolin [8], chitin-based crustacean exoskeletons [44], and carapace scutes from boxfish [7,31], all contributing to balanced penetration resistance, flexibility, lightweight, and mobility. These armor designs have different material constituents, structural designs, and specific adaptations to the functional requirements. The alligator osteoderms contain bony denser structures on the outer surface with irregular dorsal ridges and layered collagen lamellae with 100-500 µm pores inside [8]. In comparison, the armadillo osteoderms have a dark-brown keratin layer coating on top and Sharpey's fibers (non-mineralized collagen fibers) connecting the adjacent hexagonal tiles [45], while the leatherback turtle has a skin covering with jagged edges of the tiles [46]. The sutures between the individual osteoderm tiles bite with adjacent tiles for interlocking strengthening of the entire armored system, but such a mechanism also limits the motion of the tiles to $\sim \pm 15^{\circ}$. The hexagonal scutes of boxfish carapace consist of a bilayered composite similar to fish scales, with an outer high mineralized surface plate reinforced by raised struts and an inner compliant collagen base [31]. However, the sutured scutes do not have Sharpey's fibers in between, which does not have a strengthening contribution to the overall carapace but allows for accommodation of the changing pressures in the ocean habitat and growth without molting [31]. In comparison, the entire crustacean exoskeletons are developed as one piece with chitin Bouligand sheets partially mineralized by calcium carbonate for integrated protection, but the crustaceans replace the entire exoskeletons via periodic molting [44,47].

Compared with the aforementioned armored systems, the elasmoid scales have individual scales inserted into the skin forming a slanted overlapping pattern, not only enabling higher puncture resistance than the single-layered scale units [14,18] but also preventing scale tilting effectively under asymmetric puncture loading [48,49]. Previous theoretical analysis by Vernerey and Barthelat correlated the bending curvature of scaled skin with the rotation and bending of individual scales, demonstrating balanced control of the bending capability by the scale arrangement parameters, including scale length, spacing between scales, and total body length [50]. Systematic tests on different printed scale patterns give a wide spectrum on the Ashby chart, indicating an optimized choice for desired protection-compliance requirements, suggesting the advantage of having a large design space with overlapping arrangements of elasmoid scales [48].

4.2. Adaptive function of different microstructures in the individual fish scales

Previous studies on the mechanical significance of scaled armor focused primarily on the effects of scale tilting angles, mineral-to-collagen ratios, and scale dimensions. In the present study, we focused on the structural and mechanical heterogeneity within individual scales, which may suggest location-dependent material adaptations within scales.

On the outer surface of the fish scales, the circuli ridges surround the focus field. The structural difference has been reported on the arapaima scales between the exposed and covered regions, where the exposed regions have thicker but less regular mineral ridges [15] leading to enhanced fracture resistance against predatory tooth (*Pygocentrus natteri*) during penetration experiments [8,46]. Based on the comparative FE results of the scales with surface ridges (R2, R1, and F0 in **Fig. 7**) and simplified multilayers (C2, C1, and C0 in Fig. S17), the corrugations on the mineralized outer surface (including the radii sections and circuli with groves in between) have the advantage of enabling increased flexion in scales without cracking the minerals [15]. The comparison between the rostral-field models (R2 and R1) and the focus-field F0 model suggests that thicker radii sections were more effective in increasing bending flexibility than the simple circuli ridges (**Fig. 7e,h**). In addition to the general circuli features, the caudal field of the ctenoid scales aligns the surface roughness with the water current direction for hydrodynamic advantage [51].

Despite the differences of surface features in individual scales across species [8], the cross-sections of scales usually follow a common design motif: a mineralized outer region and a non-mineralized collagen inner region (Fig. 1g-i) [15,16]. This layered system in elasmoid scales enables piercing resistance under predatory bites [25,52]: with the mineralized outer layers resisting high local stress (while the surface grooves enable deformation without cracking), and the tough inner layers distributing the stress over a larger area. In addition, our results suggest the presence of local structural variations within the scales at different zones. Especially, the R2 zone near the anterior end of the scale exhibits (1) alternating multilayers (thickness of 180 µm) of high and low mineral densities and (2) fusiform-like radii sections on the exterior surface with radii grooves (thickness of 130 µm). In comparison, in R1 region close to the center of scales, the external elasmodine layer (thickness of 120 µm) is almost fully mineralized and the internal elasmodine layer (thickness of 120 µm) is non-mineralized. The comparison between the R2 and R1 models suggests that alternating layers with high and low mineralization provide increased flexibility (Fig. 7e) even with similar mineralization (ca. 67% vs. 61 % of mineralized layer thickness in the R2 and R1 models, Fig. 7a). The flexibility at different zones follows R2 > R1 > F0 (Fig. 7e), indicating increased flexibility toward the proximal edge (anterior end) of the scales. Our results suggest that this gradient in flexibility results from the microstructural architecture and different mineralization levels. The greater deformability of the rostral field scale (inserted into tissue) may facilitate flexible body movement during locomotion.

Additional mechanical significance resulting from the local structural heterogeneities within scales can be inferred from the FE results, including the out-of-plane asymmetry (concave vs. convex bending) and in-plane anisotropy (by bending on T-N and L-N planes). On one hand, the comparison between concave and convex bending suggests higher flexibility under concave bending, especially in the R2 zone, which may also suggest adaptive significance. For instance, predatory loadings induce concave bending with great deformability, which delays tissue penetration/failure during the puncture loading and increases survivability. On the other hand, scales exhibit different structures on the T-N and L-N planes (i.e., transversal and longitudinal cross-sections, respectively). In the rostral field R1 for example, the scales exhibit RS units in LL with a defined boundary between EEL and IEL on the T-N plane (Fig. 1h, modeled by the R1 model in Fig. 7a) but show surface radii grooves with triangular ridges (Fig. S4c, approximated by the F0 model in Fig. 7a), leading to different bending response on these two planes. Since the FE results suggest the deformability that R1 > F0 (Fig. 7e), we can interpret that the bulk rostral field of the individual scales should have better deformability on the T-N plane (captured by the R1 model) than the L-N plane (captured by the R0 model). In fish body locomotion, however, higher flexibility is required along the anterior-posterior bending, corresponding to the bending in the L-N plane of individual scales; the discrepancy between the bending properties of individual scales and the functional requirement of the total fish body is compensated by the overlapping scales, where the scaled skin acquires higher flexibility along the anterior-posterior direction [50].

4.3. Mineralization in elasmoid fish scales

The structural and mechanical anisotropy at different zones of the scales is closely associated with the mineralization levels. In this work, we revealed that Mandl's corpuscles may act as the precursors of mineralization in EEL during the scale mineralization process.

The growth of teleost fish scales continuously extends from the focus to the surrounding rostral and lateral fields (Fig. S7). Therefore, the mineralization in the newly formed rostral field is lower than that in the developed focus field, which is exemplified by the larger relative thickness in the highly mineralized layers (LL+EEL) in the focus field than that in the rostral field (Fig. 2g-i). The growth of the scales in thickness and size initiates by fibroblasts forming collagen fibrous sheets beneath the IEL, and the fiber orientations are controlled by the surface ridges and invaginations of the fibroblasts [53]. The mineralization in the fish scale is rather complicated and involves different mechanisms in different structural layers [53,54]: (1) The mineralization of the fish scales initiates by depositing needle-like or flasky crystallites in the EEL (at the outer surface), which was accompanied by the formation of calcification loci in cellular vesicles during the formation of this layer. (2) The subsequential mineralization of EEL inward is deposited without the mediation of those vesicles but via contact mineralization from previously mineralized regions. (3) The mineralization in the outermost LL follows a different mechanism than the mineralization in the underlying EEL, involving the secretion of a collagen-free organic matrix. (4) In the unmineralized IEL, however, random nucleation of the Mandl's corpuscles and isolated calcifications of collagen fibrils are observed in the absence of vesicles and without contacting the pre-existing calcified tissue. Especially, it would be expected that residual stress is developed within the IEL due to the local contraction of the fibrils after mineralization [55], which induces tensile residual stress in the unmineralized fibrils and thus increases the penetration resistance against predatory loading.

Here, our μ -CT characterizations at different regions suggest that Mandl's corpuscles could act as the precursors before full mineralization (Fig. 4). Specifically, in the newly formed R2 zones, the mineralized particles are small and exist more dominantly in the sublayers with longitudinal (radial) fibrils (Figs. S3b,S4b), which could correspond to the initial mineralization of EEL by calcification induced by matrix vesicles. Later, the continuous mineralization in the EEL is followed by subsequential contact mineralization, as shown in Fig. S4c,d. The isolated Mandl's corpuscles exhibit random distribution and orientations within the scale (Fig. S10), suggesting the nature of random nucleation. As the scale thickness increases, the mineralization boundary line between EEL and IEL should move inward by fusing the isolated Mandl's corpuscles. The morphological changes in these particles at R1 and R2 regions could help explain the space-filling mineralization at the front: First, the high density of Mandl's corpuscles nucleate not far away from the EEL-IEL boundary, where the small particles locate below the large ones suggesting delayed nucleation and growth (Fig. 4e, Fig. S8b,e). These mineralized particles may also have the function of bonding the adjacent fibrous laminates against delamination, yet further fracture analysis is needed to verify these assumptions (Fig. 3d-f). The particle morphologies change prominently from irregular geometries (Fig. 4e) to larger faceted crystallites (Fig. 4f) and then aggregates of multiple particles (Fig. 3e). It must be emphasized that the developed crystallites in the fibrils exhibit elongated octahedron shapes with the major axis along the fibril orientations. Yet, the mineral phase in elasmoid scales is hydroxyapatite (space group P63/m) with a hexagonal crystal system, different from the developed octahedron geometry; the correspondence between the crystallography and the particle shapes requires further detailed analysis. Later, these aggregates of Mandl's corpuscles, possibly induced by layered deposition of crystallites, fuse and fill the non-mineralized fibrils. Therefore, it may be inferred that Mandl's corpuscles are the "precursor phases" at the frontline of mineralization between the highly mineralized EEL and unmineralized IEL.

5. Conclusion

In summary, black drum fish scales are a typical example of elasmoid scales with gradient mineralization toward scale interior deposited in orthogonal collagen cross-ply laminates (*i.e.*, a highest mineralized outer layer, a highly mineralized external elasmodine layer in the middle, and a non-mineralized internal elasmodine layer). At the material level, the gradient distribution of the mineral phases is directly associated with the stepwise decrease and local oscillation in the nanoindentation modulus and hardness toward the scale interior. At the macroscopic scale of the entire scale, the tensile properties of black drum scales are similar along the longitudinal and transversal directions, correlating with the in-plane isotropy of the orthogonal cross-ply structures with circumferential and radial fibers. The deformation mechanisms in the fish scales involve the crack initiation at the circuli grooves in the limiting layer, delamination failure between the collagen fibrous laminates, and fiber bridging by the orthogonal fiber bundles across the cracked laminates.

Apart from the systematic structural-chemical-mechanical investigations of fish scales, this study highlights the structural variations at different zones within the individual scale. The newly formed anterior end of the scales consists of an elasmodine layer with alternating high and low mineralization and a limiting layer with fusiform radii sections (segmented by the surface radii interrupting the continuous circuli). Further growth leads to space-filling mineralization in the external elasmodine layer, resulting in a well-defined boundary from the unmineralized internal elasmodine layer underneath. The radii diminished at the fully developed focus field, leading to irregular ridges on

the exterior surfaces. These different structural features along the scale length enable different bending resistance, which induces the greatest deformability at the anterior end of the scale to accommodate the flexible movement of the fish body in contrast to the stiffest focus field against puncture loading.

The isolated Mandl's corpuscles at different zones map the mineralization evolution in the internal elasmodine layer. These particles nucleate randomly and are isolated in collagen fibrils, which apparently do not involve the cellular matrix vesicles or contact mineralization with previously calcified tissue. The particles are initially deposited as small irregular geometries and later develop into faceted octahedrons before coalescence, which drives the mineralization front toward the scale interior.

The insights of the structural variations within individual fish scales of black drum revealed here suggest that the fish scales are not a simple uniform tri-layer; instead, intricate microstructural control and local material heterogeneities are present, which may contribute to the animals' multi-purpose requirement, such as locomotion and protection. The results of this work could also provide inspiration for designing novel bioinspired scaled armor materials.

Declaration of competing interest

The authors declare no competing interests.

Data availability

All the data used in this work are available upon request.

Acknowledgment

L.L. gratefully acknowledges partial funding support by the United States-Israel Binational Science Foundation (BSF-2016341), National Science Foundation (DMR-1942865), and the Air Force Office of Scientific Research (FA9550-19-1-0033). In addition, the authors sincerely thank Dr. Stephen McCartney for his technical assistance with electron microscopy provided by Nanoscale Characterization and Fabrication Laboratory at Virginia Tech.

Author contributions

L.L. supervised the research. Y. T. and Z.D. designed and performed the experiments, conducted SEM measurements, and analyzed the data. Y.T. and Z. J. designed and performed the finite element simulations. All authors contributed to interpreting data, preparing manuscript, and reviewing.

References

- 1. Wegst UGK, Bai H, Saiz E, Tomsia AP, Ritchie RO. 2014 Bioinspired structural materials. *Nat. Mater.* **14**, 23–36. (doi:10.1038/nmat4089)
- 2. Meyers MA, Chen PY, Lin AYM, Seki Y. 2008 Biological materials: Structure and mechanical properties. *Prog. Mater. Sci.* **53**, 1–206. (doi:10.1016/j.pmatsci.2007.05.002)
- 3. Jia Z, Deng Z, Li L. 2022 Biomineralized materials as model systems for structural composites: 3D architecture. *Adv. Mater.* **34**, 202106259.
- 4. Martini R, Barthelat F. 2016 Stretch-and-release fabrication, testing and optimization of a flexible ceramic armor inspired from fish scales. *Bioinspiration and Biomimetics* **11**, 1–10. (doi:10.1088/1748-3190/11/6/066001)
- 5. Funk N, Vera M, Szewciw LJ, Barthelat F, Stoykovich MP, Vernerey FJ. 2015 Bioinspired Fabrication and Characterization of a Synthetic Fish Skin for the Protection of Soft Materials. *ACS Appl. Mater. Interfaces* 7, 5972–5983. (doi:10.1021/acsami.5b00258)
- 6. Vernerey FJ, Musiket K, Barthelat F. 2014 Mechanics of fish skin: A computational approach for bioinspired flexible composites. *Int. J. Solids Struct.* **51**, 274–283. (doi:10.1016/j.ijsolstr.2013.10.001)
- 7. Naleway SE, Taylor JRA, Porter MM, Meyers MA, McKittrick J. 2016 Structure and mechanical properties of selected protective systems in marine organisms. *Mater. Sci. Eng. C. Mater. Biol. Appl.* **59**, 1143–67. (doi:10.1016/j.msec.2015.10.033)
- 8. Yang W, Chen IH, Gludovatz B, Zimmermann EA, Ritchie RO, Meyers MA. 2013 Natural flexible dermal armor. *Adv. Mater.* **25**, 31–48. (doi:10.1002/adma.201202713)
- 9. Porter MM, Ravikumar N, Barthelat F, Martini R. 2017 3D-printing and mechanics of bio-inspired articulated and multi-material structures. *J. Mech. Behav. Biomed. Mater.* **73**, 114–126. (doi:10.1016/j.jmbbm.2016.12.016)
- 10. Allison PG *et al.* 2013 Mechanical properties and structure of the biological multilayered material system, Atractosteus spatula scales. *Acta Biomater.* **9**, 5289–5296. (doi:10.1016/j.actbio.2012.11.005)
- 11. Bruet BJF, Song J, Boyce MC, Ortiz C. 2008 Materials design principles of ancient fish armour. *Nat. Mater.* 7, 748–756. (doi:10.1038/nmat2231)
- 12. Rawat P, Zhu D, Rahman MZ, Barthelat F. 2020 Structural and mechanical properties of fish scales for the bio-inspired design of flexible body armors: A review. *Acta Biomater*. (doi:10.1016/j.actbio.2020.12.003)
- 13. Hossain MS, Ebrahimi H, Ghosh R. 2022 Fish scale inspired structures a review of materials, manufacturing and models. *Bioinspir. Biomim.* **17**, 061001.
- 14. Zhu D, Szewciw L, Vernerey F, Barthelat F. 2013 Puncture resistance of the scaled skin from striped bass: Collective mechanisms and inspiration for new flexible armor designs. *J. Mech. Behav. Biomed. Mater.* **24**, 30–40. (doi:10.1016/j.jmbbm.2013.04.011)
- 15. Meyers MA, Lin YS, Olevsky EA, Chen PY. 2012 Battle in the Amazon: Arapaima versus piranha. *Adv. Eng. Mater.* **14**. (doi:10.1002/adem.201180027)
- 16. Lin YS, Wei CT, Olevsky EA, Meyers MA. 2011 Mechanical properties and the laminate structure of Arapaima gigas scales. *J. Mech. Behav. Biomed. Mater.* **4**, 1145–1156. (doi:10.1016/j.jmbbm.2011.03.024)
- 17. Arola D, Murcia S, Stossel M, Pahuja R, Linley T, Devaraj A, Ramulu M, Ossa EA, Wang J. 2018 The limiting layer of fish scales: Structure and properties. *Acta Biomater*. **67**, 319–330. (doi:10.1016/j.actbio.2017.12.011)
- 18. Browning A, Ortiz C, Boyce MC. 2013 Mechanics of composite elasmoid fish scale assemblies and their bioinspired analogues. *J. Mech. Behav. Biomed. Mater.* **19**, 75–86. (doi:10.1016/j.jmbbm.2012.11.003)
- 19. Ikoma T, Kobayashi H, Tanaka J, Walsh D, Mann S. 2003 Microstructure, mechanical, and biomimetic properties of fish scales from Pagrus major. *J. Struct. Biol.* **142**, 327–333. (doi:10.1016/S1047-8477(03)00053-4)
- 20. Marino Cugno Garrano A, La Rosa G, Zhang D, Niu LN, Tay FR, Majd H, Arola D. 2012 On the

- mechanical behavior of scales from Cyprinus carpio. *J. Mech. Behav. Biomed. Mater.* **7**, 17–29. (doi:10.1016/j.jmbbm.2011.07.017)
- 21. Zhu D, Ortega CF, Motamedi R, Szewciw L, Vernerey F, Barthelat F. 2012 Structure and mechanical performance of a 'modern' fish scale. *Adv. Eng. Mater.* **14**. (doi:10.1002/adem.201180057)
- 22. Chen PY *et al.* 2012 Predation versus protection: Fish teeth and scales evaluated by nanoindentation. *J. Mater. Res.* 27, 100–112. (doi:10.1557/jmr.2011.332)
- 23. Khayer Dastjerdi A, Barthelat F. 2015 Teleost fish scales amongst the toughest collagenous materials. *J. Mech. Behav. Biomed. Mater.* **52**, 95–107. (doi:10.1016/j.jmbbm.2014.09.025)
- 24. Rudykh S, Ortiz C, Boyce MC. 2015 Flexibility and protection by design: Imbricated hybrid microstructures of bio-inspired armor. *Soft Matter* **11**, 2547–2554. (doi:10.1039/c4sm02907k)
- 25. Vernerey FJ, Barthelat F. 2010 On the mechanics of fishscale structures. *Int. J. Solids Struct.* 47, 2268–2275. (doi:10.1016/j.ijsolstr.2010.04.018)
- 26. Feng X, Wenxue Z, Yuanyuan Q, Huaibin K. 2015 Optimization of demineralization on Cyprinus carpio haematopterus scale by response surface methodology. *J. Food Sci. Technol.* **52**, 1684–1690. (doi:10.1007/s13197-013-1164-y)
- 27. Fan X. 2013 Mechanical Characterization of Hydroxyapatite, Thermoelectric Materials and Doped Ceria. Michigan State University. See https://etd.lib.msu.edu/islandora/object/etd%3A802/datastream/OBJ/view.
- 28. Proestaki M, Ogren A, Burkel B, Notbohm J. 2019 Modulus of Fibrous Collagen at the Length Scale of a Cell. *Exp. Mech.* **59**, 1323–1334. (doi:10.1007/s11340-018-00453-4)
- 29. Schönbörner AA, Meunier FJ, Castanet J. 1981 The fine structure of calcified Mandl's corpuscles in teleost fish scales. *Tissue Cell* 13, 589–597. (doi:10.1016/0040-8166(81)90029-X)
- 30. Sankar S, Sekar S, Mohan R, Rani S, Sundaraseelan J, Sastry TP. 2008 Preparation and partial characterization of collagen sheet from fish (Lates calcarifer) scales. *Int. J. Biol. Macromol.* **42**, 6–9. (doi:10.1016/j.ijbiomac.2007.08.003)
- 31. Yang W, Naleway SE, Porter MM, Meyers MA, McKittrick J. 2015 The armored carapace of the boxfish. *Acta Biomater.* **23**, 1–10. (doi:10.1016/j.actbio.2015.05.024)
- 32. Long JH, Hale ME, McHenry MJ, Westneat MW. 1996 Functions of fish skin: Flexural stiffness and steady swimming of longnose gar Lepisosteus osseus. *J. Exp. Biol.* **199**, 2139–2151.
- 33. Szewciw L, Barthelat F. 2017 Mechanical properties of striped bass fish skin: Evidence of an exotendon function of the stratum compactum. *J. Mech. Behav. Biomed. Mater.* **73**, 28–37. (doi:10.1016/j.jmbbm.2016.09.031)
- 34. Yang W *et al.* 2014 Protective role of Arapaima gigas fish scales: Structure and mechanical behavior. *Acta Biomater.* **10**, 3599–3614. (doi:10.1016/j.actbio.2014.04.009)
- 35. Torres FG, Troncoso OP, Nakamatsu J, Grande CJ, Gómez CM. 2008 Characterization of the nanocomposite laminate structure occurring in fish scales from Arapaima Gigas. *Mater. Sci. Eng. C* **28**, 1276–1283. (doi:10.1016/j.msec.2007.12.001)
- 36. Murcia S, Lavoie E, Linley T, Devaraj A, Ossa EA, Arola D. 2017 The natural armors of fish: A comparison of the lamination pattern and structure of scales. *J. Mech. Behav. Biomed. Mater.* **73**, 17–27. (doi:10.1016/j.jmbbm.2016.09.025)
- 37. Zhu D, Barthelat F, Vernerey F. 2013 Intricate Multiscale Mechanical Behaviors of Natural Fish-Scale Composites. In *Handbook of Micromechanics and Nanomechanics*, pp. 975–994. (doi:10.4032/9789814411240)
- 38. Zylberberg L, Bereiter-Hahn J, Sire JY. 1988 Cytoskeletal organization and collagen orientation in the fish scales. *Cell Tissue Res.* **253**, 597–607. (doi:10.1007/BF00219750)
- 39. Gil-Duran S, Arola D, Ossa EA. 2016 Effect of chemical composition and microstructure on the mechanical behavior of fish scales from Megalops Atlanticus. *J. Mech. Behav. Biomed. Mater.* **56**, 134–145. (doi:10.1016/j.jmbbm.2015.11.028)

- 40. Giraud MM, Castanet J, Meunier FJ, Bouligand Y. 1978 The fibrous structure of coelacanth scales: A twisted 'Plywood'. *Tissue Cell* **10**, 671–686. (doi:10.1016/0040-8166(78)90054-X)
- 41. Sherman VR, Quan H, Yang W, Ritchie RO, Meyers MA. 2017 A comparative study of piscine defense: The scales of Arapaima gigas, Latimeria chalumnae and Atractosteus spatula. *J. Mech. Behav. Biomed. Mater.* **73**, 1–16. (doi:10.1016/j.jmbbm.2016.10.001)
- 42. Naleway SE, Porter MM, McKittrick J, Meyers MA. 2015 Structural Design Elements in Biological Materials: Application to Bioinspiration. *Adv. Mater.* 27, 5455–5476. (doi:10.1002/adma.201502403)
- 43. Zimmermann EA, Gludovatz B, Schaible E, Dave NKN, Yang W, Meyers MA, Ritchie RO. 2013 Mechanical adaptability of the Bouligand-type structure in natural dermal armour. *Nat. Commun.* **4**, 1–7. (doi:10.1038/ncomms3634)
- 44. Fabritius H-O *et al.* 2016 Functional adaptation of crustacean exoskeletal elements through structural and compositional diversity: a combined experimental and theoretical study. *Bioinspir. Biomim.* **11**, 055006. (doi:10.1088/1748-3190/11/5/055006)
- 45. Chen IH, Kiang JH, Correa V, Lopez MI, Chen PY, McKittrick J, Meyers MA. 2011 Armadillo armor: Mechanical testing and micro-structural evaluation. *J. Mech. Behav. Biomed. Mater.* **4**, 713–722. (doi:10.1016/j.jmbbm.2010.12.013)
- 46. Yang W, Chen IH, McKittrick J, Meyers MA. 2012 Flexible dermal armor in nature. *Jom* **64**, 475–485. (doi:10.1007/s11837-012-0301-9)
- 47. Raabe D, Sachs C, Romano P. 2005 The crustacean exoskeleton as an example of a structurally and mechanically graded biological nanocomposite material. *Acta Mater.* **53**, 4281–4292. (doi:10.1016/j.actamat.2005.05.027)
- 48. Martini R, Balit Y, Barthelat F. 2017 A comparative study of bio-inspired protective scales using 3D printing and mechanical testing. *Acta Biomater.* **55**, 360–372. (doi:10.1016/j.actbio.2017.03.025)
- 49. Martini R, Barthelat F. 2016 Stability of hard plates on soft substrates and application to the design of bioinspired segmented armor. *J. Mech. Phys. Solids* **92**, 195–209. (doi:10.1016/j.jmps.2016.04.009)
- 50. Vernerey, F. J.; Barthelat, F. 2014 Skin and Scales of Teleost Fish: Simple Structure but High Performance and Multiple Functions. *J. Mech. Phys. Solids* **68**, 66–76.
- 51. Sudo S, Tsuyuki K, Ito, Yoshiyasu I, Ikohagi T. 2002 A study on the surface shape of fish scales. *Japan Soc. Mech. Eng. Int. J.* **45**, 1100–1105. (doi:10.1299/jsmec.45.1100)
- 52. Ortiz C, Boyce MC. 2008 Bioinspired Structural Materials. *Science*. **319**, 1053–1054. (doi:10.1126/science.1154295)
- 53. Onozato H, Watabe N. 1979 Studies on fish scale formation and resorption. *Cell Tissue Res.* **201**, 409–422. (doi:10.1007/bf00236999)
- 54. Schönbörner AA, Boivin G, Baud CA. 1979 The mineralization processes in Teleost fish scales. *Cell Tissue Res.* **202**, 203–212. (doi:10.1007/BF00232235)
- 55. Ping H, Wagermaier W, Horbelt N, Scoppola E, Li C, Werner P, Fu Z, Fratzl P. 2022 Mineralization generates megapascal contractile stresses in collagen fibrils. *Science*. **376**, 188–192. (doi:10.1126/science.abm2664)